

Trabecular Bone Structure Analysis in the Osteoporotic Spine Using a Clinical In Vivo Setup for 64-Slice MDCT Imaging: Comparison to μ CT Imaging and μ FE Modeling

Ahi S. Issever,^{1,2} Thomas M. Link,² Marie Kentenich,^{1,2} Patrik Rogalla,¹ Karsten Schwieger,³ Markus B. Huber,² Andrew J. Burghardt,² Sharmila Majumdar,² and Gerd Diederichs^{1,2}

ABSTRACT: Assessment of trabecular microarchitecture may improve estimation of biomechanical strength, but visualization of trabecular bone structure in vivo is challenging. We tested the feasibility of assessing trabecular microarchitecture in the spine using multidetector CT (MDCT) on intact human cadavers in an experimental in vivo-like setup. BMD, bone structure (e.g., bone volume/total volume = BV/TV; trabecular thickness = Tb.Th; structure model index = SMI) and bone texture parameters were evaluated in 45 lumbar vertebral bodies using MDCT (mean in-plane pixel size, 274 μm^2 ; slice thickness, 500 μm). These measures were correlated with structure measures assessed with μ CT at an isotropic spatial resolution of 16 μm and to microfinite element models (μ FE) of apparent modulus and stiffness. MDCT-derived BMD and structure measures showed significant correlations to the density and structure obtained by μ CT (BMD, $R^2 = 0.86$, $p < 0.0001$; BV/TV, $R^2 = 0.64$, $p < 0.0001$; Tb.Th, $R^2 = 0.36$, $p < 0.01$). When comparing μ CT-derived measures with μ FE models, the following correlations ($p < 0.001$) were found for apparent modulus and stiffness, respectively: BMD ($R^2 = 0.58$ and 0.66), BV/TV ($R^2 = 0.44$ and 0.58), and SMI ($R^2 = 0.44$ and 0.49). However, the overall highest correlation ($p < 0.001$) with μ FE app. modulus ($R^2 = 0.75$) and stiffness ($R^2 = 0.76$) was achieved by the combination of QCT-derived BMD with the bone texture measure Minkowski Dimension. In summary, although still limited by its spatial resolution, trabecular bone structure assessment using MDCT is overall feasible. However, when comparing with μ FE-derived bone properties, BMD is superior compared with single parameters for microarchitecture, and correlations further improve when combining with texture measures.

J Bone Miner Res 2009;24:1628–1637. Published online on March 30, 2009; doi: 10.1359/JBMR.090311

Key words: multidetector CT, μ CT, trabecular bone, spine, structure analysis

Address correspondence to: Ahi Sema Issever, MD, Department of Radiology, Charité Campus Mitte, Universitätsmedizin Berlin, Berlin, Germany, E-mail: ahi-sema.issever@charite.de

INTRODUCTION

ALTHOUGH IT IS known that BMD measurements are limited in their ability to predict fracture risk^(1–3) and quantify the outcome of osteoporosis treatment,^(4–6) DXA and QCT remain the established methods in current osteoporosis management. Nevertheless, aspects of bone quality beyond BMD have been shown to be important predictors of bone fragility.^(7,8) Among these, measures of trabecular bone microarchitecture contribute independent information to statistical models for identifying subjects at increased fracture risk.^(9–11) Thus, depiction and analysis of trabecular bone structure will play an essential role in future concepts of osteoporosis diagnosis and monitoring. Many imaging modalities have been used for trabecular bone structure analysis, and μ CT—which is capable of 6- μm isotropic resolutions—may be considered the most widely used current imaging gold standard. However, μ CT

imaging is presently restricted to ex vivo and preclinical in vivo imaging applications. In vivo human trabecular bone imaging is feasible at peripheral skeletal sites. However, the spatial resolution achieved is still substantially lower compared with μ CT. High-resolution pQCT (HR-pQCT) of the radius and the tibia is currently the most advanced technique and performed with an isotropic resolution of 82 μm .⁽¹²⁾ High-resolution MRI of the same sites—using high-field 3-T MRI systems—provides $156 \times 156 \mu\text{m}^2$ in plane pixel size.⁽¹³⁾ However, imaging central sites such as the spine and the proximal femur still remain challenging. Recently, preliminary findings have suggested microstructural indices determined from multidetector CT (MDCT) images have the ability to differentiate patients with and without vertebral fractures⁽¹⁴⁾ and in quantifying therapeutic effects.⁽¹⁵⁾

To the best of our knowledge, no studies have been performed assessing how well apparent vertebral bone structure obtained from in vivo MDCT reflects the true trabecular bone structure. In this study, intact human

The authors state that they have no conflicts of interest.

¹Department of Radiology, Charité Campus Mitte, Universitätsmedizin Berlin, Berlin, Germany; ²Department of Radiology and Biomedical Imaging, Musculoskeletal and Quantitative Imaging Research Group, University of California, San Francisco, California, USA; ³AO Research Institute, Department of Research Services, Davos, Switzerland.

cadavers were imaged using an in vivo MDCT imaging protocol to (1) evaluate the accuracy of trabecular bone structure analysis performed on spinal MDCT images using μ CT as a reference, (2) compare trabecular structure measures with biomechanical properties obtained by microfinite element modeling (μ FE), and (3) evaluate texture analysis as an alternative method to quantify trabecular structure and compare with μ FE-derived biomechanical properties.

MATERIALS AND METHODS

Specimens

This study was performed in 15 complete human cadavers (10 male and 5 female; mean age, 86 yr; age range, 67–102 yr). Before death, all individuals had given signed consent to dedicate their bodies to the Institute of Anatomy, Charité Campus Mitte, Universitätsmedizin Berlin, Berlin, Germany. Eight donors had died of complications related to coronary heart disease, three from pneumonia, one from complications related to a benign cerebral tumor, and one from a stroke. The cause of death for two individuals was unknown. The specimens were stored in a refrigerated room (4°C), and MDCT imaging was performed after all forensic investigations were completed (on average 5 days postmortem).

After the MDCT imaging, the cadavers were fixed in a 4% paraformaldehyde solution, and the lumbar vertebral bodies L₁–L₃ were extracted. A water-cooled diamond tipped coring drill bit was used to extract cylindrical cores (9 mm diameter) from the three vertebral bodies. The drill was manually placed in the center of the superior endplate, and the core was obtained by drilling through the entire vertebral body (height 20–45 mm). The cores and the specimen were stored within a 4% paraformaldehyde solution at room temperature. Criteria for exclusion from the study were evidence of prior fracture and osteolytic or osteoblastic changes suggesting osseous metastases.

Imaging techniques

MDCT imaging: MDCT measurements were performed on a 64 multidetector row CT scanner (Aquilion 64; Toshiba, Otawara, Japan) with the cadaver positioned in supine position and the arms lifted above the head consistent with the standard patient scanning protocol.

Standard whole body CT scan: To identify vertebral fractures or possible malignant osseous involvement of the entire spine, standard axial CT scans of the thorax, abdomen, and pelvis were performed. A tube voltage of 120 kVp with an automatically dose modulated tube current and a rotation time of 0.5 s was used. The slice thickness was 0.5 mm, and the slice increment was 0.3 mm. Images were reconstructed using a standard body kernel (FC13).

QCT for BMD assessment: To quantify BMD, QCT measurements were performed (120 kVp, 50 mA). A hydroxyapatite (HA) calibration phantom consisting of five tubular inserts with varying concentrations of HA (0, 50, 100, 150, and 200 mg/cm³) was placed underneath the

cadavers. A lateral scout scan was performed for localization of the tomographic scan position. This consisted of an 8-mm section acquired parallel to the endplates in the center of the L₁, L₂, and L₃ vertebral bodies.

High-resolution protocol: Three different scan protocols covering the lumbar spine segment from L₁–L₃ were implemented: (A) 80 kVp, 150 mA; (B) 120 kVp, 250 mA, and (C) 135 kVp, 350 mA. For all protocols, a slice thickness of 0.5 mm and increment of 0.3 mm was obtained. The rotation time was set to 0.5 s. To ensure central positioning of the lumbar spine within the scanner and to ensure full coverage of the calibration phantom, an individually adapted field of view (FOV) with an average size of 14 cm (range, 10–22 cm) was chosen. A standard matrix size of 512 × 512 pixels, yielding an average in plane pixel size of 0.274 mm² (range, 0.195–0.433 mm²) was applied. Images were reconstructed using a bone reconstruction kernel (FC30).

μ CT imaging: As a standard of reference, μ CT images were acquired using a desktop ex vivo μ CT system (μ CT-40; Scanco Medical, Bassersdorf, Switzerland).^(16,17) The technical details and principles of this imaging device have been previously described in detail.⁽¹⁸⁾ For our purposes, we acquired data using a source potential of 70 kVp and a current of 114 mA. Five hundred projection images were collected, spanning 180°, with each projection sampled for 250 ms. The projections were reconstructed across a 1024 × 1024 matrix spanning a 16.4-mm FOV and resulting in an isotropic nominal resolution of 16 μ m. For each core, the scan range was defined on the lateral scout view to cover the central 10 mm (625 axial sections; approximate scan time 4.5 h; Fig. 1A). The specimens were immersed in a saline solution during imaging.

High-resolution pQCT: For image registration purposes, as described below, the cored specimens (vertebral bodies containing a void at the core site) were imaged at an isotropic 246- μ m voxel size using an HR-pQCT system (XtremeCT; Scanco Medical). Specimen positioning was done consistent with the MDCT scan, and the scan range covered the entire vertebral body. The following scan settings were used: source potential, 60 kVp; tube current, 900 μ A; integration time, 300 ms.

Image co-registration

A cylindrical volume of interest (VOI; 8 mm diameter, 10 mm height) for each core was defined on the μ CT images. To locate the μ CT-defined VOI in the MDCT scans, the cored specimens (vertebral body with coring “hole”) were rescanned at an isotropic 246- μ m voxel size using a HR-pQCT scanner system (XtremeCT; Scanco Medical). The HR-pQCT and MDCT data sets were co-registered using the image processing software OsiriX v.2.7.5 (The OsiriX Foundation, Geneva, Switzerland). The isotropic HR-pQCT data set was reformatted in the same spatial orientation as the MDCT images were scanned, resulting in matched slices. After the central slice of the HR-pQCT dataset was identified with respect to the central slice of the MDCT scan, the location of the cylinder was determined by aligning reference lines at anatomical landmarks, such

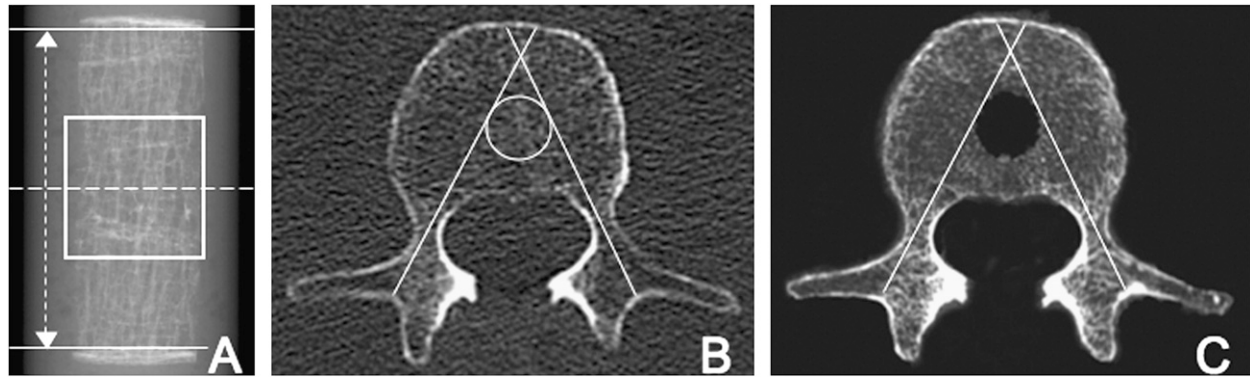


FIG. 1. (A) Lateral μ CT scout view of a representative core. The central VOI (10-mm white outlined box) was defined by (i) measuring the distance between the upper and lower margins of where the trabecular bone network starts (solid white lines) and (ii) identifying the central slice (dotted line) using the following formula: $(\text{upper}_{\text{margin}} - \text{lower}_{\text{margin}})/2$. The scan (625 axial slices, 10 mm) was set to start 5 mm above the central slice. An axial MDCT section of the intact vertebral body acquired with protocol B is shown in B. The matching HR-pQCT section of the vertebral body with core defect after reformation is depicted in C. Alignment of reference lines at reproducible anatomical landmarks is used to locate and define the volume of interest within the MDCT image.

as the pedicels, the transverse and spinosus processes, and the vertebral body. Final confirmation was performed by visual inspection of characteristics in the trabecular network and surrounding cortex (Figs. 1B and 1C).

Image analysis

Spinal fracture index: Using a modified spinal fracture index, as introduced by Genant et al.,⁽¹⁹⁾ the fracture status of T₁ to L₅ were assessed semiquantitatively from the sagittal CT reconstructions. Fractures (grade I, II, and III) were defined as a reduction >20% in the anterior or mid-vertebral height. The identification of vertebral bodies meeting the exclusion criteria was performed in consensus by two radiologists.

BMD: BMD acquired by MDCT: Mean Hounsfield unit (HU) values for each individual calibration tube (HA 0, 50, 100, 150, 200 mg/cm³) were calculated for each donor and each scan (QCT, MDCT). Linear regression analysis was used to derive scan-specific equations to calibrate HU to BMD units. Mean HU values were determined for the following VOIs: (1) anterior three fourths of the vertebral body in the QCT scans and (2) in the 9-mm cylindrical VOI in the MDCT scan corresponding to the registered core site. MDCT scan, standard BMD, and BMD of the VOI (vBMD) was calculated as a concentration of HA (mg/cm³). All regions of interest were manually placed in consensus by two radiologists.

BMD acquired by μ CT: Calibration of the reconstructed grayscale attenuation values of the VOI against mineral density was performed using a phantom composed of five cylinders of HA–resin mixtures with a range of mineral concentrations (0, 100, 200, 400, and 800 mg HA/cm³), where 0 mg HA/cm³ represents a soft tissue equivalent background devoid of mineral. The mean attenuation value for each VOI was calculated, and individual linear relationships were determined against the known mineral concentrations: $[\text{HA}] = m\mu + b$, where m and b represent the slope and intercept relating HA concentration ($[\text{HA}]$ in mg HA/cm³) to linear attenuation (μ).

Trabecular structure analysis: MDCT: Structure analysis of the MDCT images was performed using in-house

developed image analysis software, programmed in IDL (RSI, Boulder, CO, USA). For threshold definition purposes, six different thresholds corresponding to HA density values of 50, 100, 150, 200, 250, and 300 HA mg/cm³ were applied to each MDCT data set. The HA density values were reconverted to HU by back-calibration using the manufacturer's calibration phantom. Structural indices—as explained later—were calculated at each threshold for each MDCT data set and compared with the corresponding structure indices determined by μ CT. An optimal threshold was identified as the HA density level that yielded the highest combination of correlation coefficients (see Results section). After image binarization, apparent trabecular structure measures were derived, as previously described in detail by Majumdar and Genant.⁽²⁰⁾ The trabecular structure measures denoted “apparent” (app.) because of the limited spatial resolution of MDCT. Thus, app. bone volume/total volume (BV/TV), app. trabecular number (Tb.N), thickness (Tb.Th), and separation (Tb.Sp) were computed. Briefly, app. BV/TV was calculated as the ratio of the total number of object pixels representing the bone phase to the total number of pixels in the volume of interest. The total number of black and white pixel edges that cross a set of parallel rays at a given angle θ through the image were counted, and a measure of the mean intercept length was computed as the ratio between the total area of the bright pixels and one half the number of edges. The mean value of the intercept length for all angles provided the width of the bright pixels and was defined as app. Tb.Th. From these measurements of app. BV/TV and app. Tb.Th, app. Tb.N (area fraction of bright pixels/app. Tb.Th) and app. Tb.Sp ($[1/\text{app. Tb.N}] - \text{app. Tb.Th}$) were calculated.

μ CT: The μ CT gray level images were binarized into a bone and marrow phase by first applying a low-pass Gaussian filter (width = 1.2, support = 2) to remove noise and using a global threshold. The global threshold was calculated for each specimen using a common adaptive iterative method on a specific specimen-based histogram analysis.⁽²¹⁾ Density measures and the following structural

parameters were calculated: BV/TV, Tb.N, Tb.Th, Tb.Sp, connectivity density (Conn.D),⁽²²⁾ and structure model index (SMI).⁽²³⁾ The underlying assumption to this method is that the histogram intensity distribution is bimodal, expressing a bone and background peak. The midpoint between the two peaks was used as the threshold value. BV/TV was derived through simple voxel counting. Calculation of Tb.N, Tb.Th, and Tb.Sp was performed without model assumptions as direct measures.⁽²⁴⁾

Trabecular texture analysis: Using the MDCT images, 2D texture indices developed in house on a MATLAB platform (The MathWorks, Natick, MA, USA) were calculated. The gray level pixels contained in each MDCT VOI were rescaled to 256 gray level values (minimum-maximum-scaling), and the following texture measures categories were computed: Minkowski dimension, Minkowski functionals, gray level co-occurrence matrix, third-order gray level co-occurrence matrix, and scaling index method.

Fractal properties were assessed with the global Minkowski dimension (MD)^(25,26) a robust estimator based on morphological operations. For the calculation, the structuring element was a square (MD_{squa}) and a disk (MD_{disk}). In addition, anisotropic structuring elements were used pointing in four different directions (0°, 90°, 45°, 135°), and the mean and SD of those four directions were calculated (MD_{aniso} and MD_{aniso,std}, respectively).

Two optimized parameters based on the Minkowski functionals (MFs)^(27,28) were applied that extract topological information from the texture maps. A 2D image is represented by three MFs: area (MF_{area}), perimeter (MF_{perim}), and the Euler number (MF_{euler}). These three MFs are functions of the gray level threshold, which characterizes the underlying topological features of the image texture. Three thresholds were used in this analysis based on the VOI's gray level histogram: the mean and the two quantiles: qu25 (25%) and qu75 (75%).

The gray level co-occurrence matrix (GLCM)⁽²⁹⁾ estimates the joint probability of two gray level pixel for a given pixel spacing and direction, and the third-order gray level co-occurrence matrix (TOGLCM)⁽³⁰⁾ calculates the joint probability of three gray level pixels. To extract textural information from the GLCM and TOGLCM, we derived the statistical features contrast, correlation, homogeneity, absolute value, entropy, energy, and large number emphasis (LNE).

Local scaling properties of the texture maps were estimated with the scaling index method,⁽³¹⁾ which was previously developed for the analysis of atomic force microscope images⁽³²⁾ and automated detection of melanoma.⁽³³⁾ Applying SIM can be regarded as an image transformation that assigns each pixel gray level (original image) a local scaling property (SIM image) that depends on the neighboring pixels within a given scale. The histogram of the resulting SIM image contains nonlinear structure and texture information and can be used to extract texture features. Here, the mean, median and standard deviation were calculated for each SIM image (SIM_{mean}, SIM_{median}, SIM_{stdev}) for scales $r = 4, 6, 8$.

μFE modeling

Apparent elastic biomechanical properties were determined for each specimen by linear μFE analysis. Each cylindrical binary μCT image set was converted to a mesh of isotropic brick elements using a voxel conversion technique,⁽³⁴⁾ and each element was assigned an elastic modulus of 10 GPa⁽³⁵⁾ and a Poisson's ratio of 0.3.⁽³⁶⁾ On average, the models were composed of 6,166,508 elements. A uniaxial compression test in the axial direction (superior-inferior) was performed with an applied strain of 1%. An iterative solver (Scanco FE Software v1.12; Scanco Medical) was used to compute reaction forces at the superior and inferior ends of the cylinder for the prescribed boundary conditions. App. modulus (MPa) is calculated as app. stress divided by app. strain, whereas stiffness (MPa) is calculated as the total reaction force at the boundary divided by the displacement. The model computations were performed at the UCSF/QB3 Shared Computing Facility—a mixed architecture linux grid comprised of 1300 processor nodes. The models required an average of 83.9 CPU hours.

Statistics

The means and SDs were calculated for the density, structure, and texture parameters obtained by μCT and MDCT, as well as for the biomechanical parameters as obtained by μFE. A paired, two-tailed Student's *t*-test was used to determine the statistical significance of differences between MDCT- and μCT-derived structural parameters. Parameters derived from MDCT, μCT, and μFE were correlated using a linear regression analysis computing coefficient of determination (R^2) values, with R^2 values of 0.00–0.29 being considered as little, 0.30–0.49 as low, 0.50–0.69 as moderate, 0.70–0.89 as high, and 0.90–1.00 as very high correlations. A multivariate linear regression model with stepwise mixed selection was used to test the ability of a combination of BMD, structure, and texture indices to predict μFE-derived biomechanical properties. The level of significance was set at 5% ($p < 0.05$); values that were significant at a 0.1% level ($p < 0.001$) were defined as highly significant. All calculations were performed with JMP software (SAS Institute, Cary, NC, USA).

RESULTS

Spinal fracture index

In 8 of the 15 body donors (53%), vertebral deformities were detected: 1 grade I, 6 grade II, and 23 grade III deformities. On average, there were 3.75 vertebral deformities per fracture patient. Of these fractures, 12 were located in L₁–L₃. As a result, 33 of the 45 total vertebrae were ultimately included in the study.

BMD

Using standard single-slice QCT, the mean BMD of L₁–L₃ within the 15 body donors was $81.60 \pm 29.62 \text{ mg/cm}^3$ (range, 41.22–123.89 mg/cm³). Eight subjects had BMD values <80.00 mg/cm³ and therefore were considered

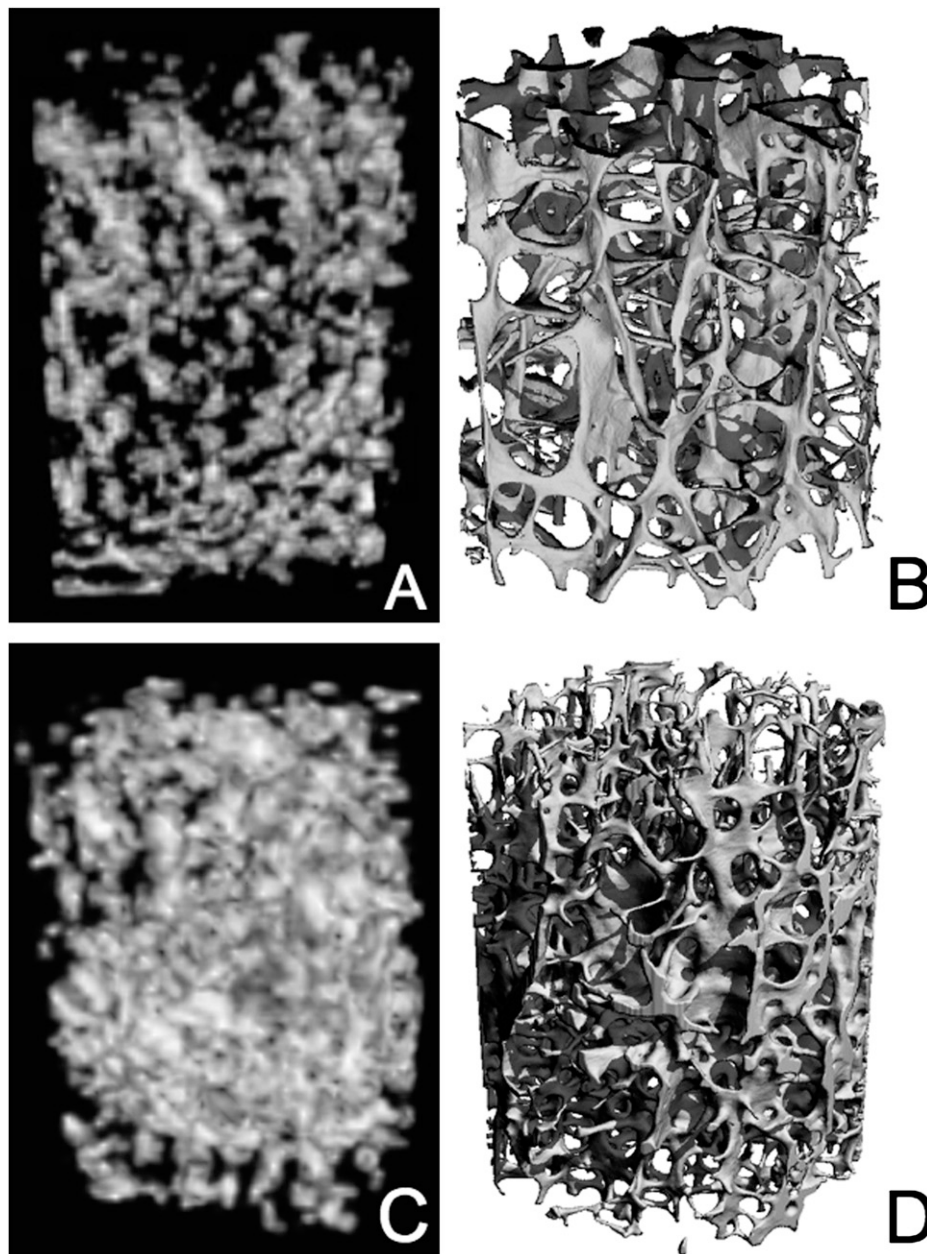


FIG. 2. 3D reconstructions from MDCT (A and C) and μ CT (B and D) image datasets of two body donors (A and B, osteoporotic $\text{BMD}_{\text{OCT}} = 46.41 \text{ mg/cm}^3$; C and D, normal $\text{BMD}_{\text{OCT}} = 109.60 \text{ mg/cm}^3$) are depicted.

osteoporotic according to the definition given by Felsenberg and Gowin.⁽³⁷⁾ Five of the eight osteoporotic donors were found to have vertebral fractures.

The mean vBMD values as assessed by MDCT protocols A, B, and C were 104.52 ± 38.53 , 100.36 ± 43.44 , and $97.35 \pm 44.49 \text{ mg/cm}^3$, respectively. MDCT-derived vBMD showed moderate correlations to standard QCT-derived BMD (A: $R^2 = 0.51$; B: $R^2 = 0.67$; C: $R^2 = 0.69$; $p < 0.0001$). Student's *t*-test showed that vBMD values as assessed with protocol C showed no statistical difference compared with standard QCT-derived BMD values ($p > 0.05$).

The mean vBMD determined by μ CT was $92.79 \pm 29.64 \text{ mg/cm}^3$. MDCT- and μ CT-derived vBMD measures showed moderate to high correlations ($R^2 = 0.64$ for A and

$R^2 = 0.86$ for B and C; $p < 0.0001$) with Student's *t*-test values $p > 0.05$.

Global threshold definition for the MDCT datasets

MDCT-derived app. BV/TV and app. Tb.Th are the two structure measures that showed the most significant correlations ($p < 0.001$) with the corresponding μ CT measures for all protocols and all applied thresholds. With increasing threshold values, the correlations for Tb.Th increased steadily, whereas BV/TV reached a peak at ~ 150 and 200 HA mg/cm^3 . With Tb.N and Tb.Sp included, the optimal combination of the most significant correlations was found at the 150-HA mg/cm^3 threshold level.

TABLE 1. μ CT-Derived Trabecular Structure Measures and MDCT-Derived Apparent Trabecular Structure Measures Expressed as Mean \pm SD

<i>N</i> = 33	μ CT	MDCT protocol		
		<i>A</i>	<i>B</i>	<i>C</i>
vBMD (mg/cm ³)	92.79 \pm 29.64	104.52 \pm 38.53	100.36 \pm 43.44	97.35 \pm 44.49
BV/TV (%)	8 \pm 2	45 \pm 4*	36 \pm 10*	32 \pm 12*
Tb.Th (mm)	0.16 \pm 0.02	0.52 \pm 0.07*	0.50 \pm 0.13*	0.50 \pm 0.17*
Tb.Sp (mm)	1.13 \pm 0.19	0.64 \pm 0.06*	0.92 \pm 0.24*	1.15 \pm 0.40
Tb.N (1/mm)	0.85 \pm 0.14	0.87 \pm 0.06	0.72 \pm 0.09*	0.64 \pm 0.11*
Conn. D (1/mm ³)	2.16 \pm 1.09	—	—	—
SMI	2.09 \pm 0.27	—	—	—

In addition, two-tailed paired *t*-test was performed to evaluate the statistically significant difference between μ CT- and MDCT-derived measures and between the MDCT protocols.

MDCT protocol A: 80 kVp, 150 mA; B: 120 kVp, 250 mA; C: 135 kVp, 350 mA.

* *p* < 0.05: *t*-test values between μ CT and MDCT measures.

TABLE 2. Coefficients of Determination (R^2) Between MDCT- and μ CT-Derived Measures

<i>N</i> = 33	MDCT protocol vs. μ CT		
	<i>A</i>	<i>B</i>	<i>C</i>
vBMD	0.64*	0.86*	0.86*
BV/TV	0.52*	0.64*	0.60*
Tb.Th	0.36 [†]	0.32 [†]	0.32 [†]
Tb.Sp	NS	0.25 [‡]	0.19 [‡]
Tb.N	NS	0.15 [‡]	0.13 [‡]

MDCT protocol A: 80 kVp, 150 mA; B: 120 kVp, 250 mA; C: 135kVp, 350 mA.

* *p* < 0.0001.

[†] *p* < 0.01.

[‡] *p* < 0.05.

NS, nonsignificant.

TABLE 3. Coefficients of Determination R^2 Between μ CT-Derived Measures and MDCT-Derived Texture Measures

<i>N</i> = 33 μ CT	MDCT protocol			
	Texture measure	<i>A</i>	<i>B</i>	<i>C</i>
vBMD	SIM _{quan75.r8}	0.60*	0.60*	0.70*
BV/TV	SIM _{quan75.r8}	0.46*	0.46*	0.60*
Tb.Th	MD _{deg45}	0.38 [†]	0.38 [†]	0.42 [†]
Tb.Sp	TOGLCM _{LNE}	NS	0.44*	0.40 [†]
Tb.N	TOGLCM _{LNE}	NS	0.40 [†]	0.39 [†]
Conn.D	TOGLCM _{LNE}	NS	0.28 [‡]	0.31 [‡]
SMI	MF _{aera.qu25}	NS	0.13 [‡]	0.15 [‡]

MDCT protocol A: 80 kVp, 150 mA; B: 120 kVp, 250 mA; C: 135kVp, 350 mA.

* *p* < 0.0001.

[†] *p* < 0.01.

[‡] *p* < 0.05.

NS, nonsignificant.

Accordingly, this was defined as the global threshold for further evaluation.

Structural parameters assessed with MDCT and μ CT

Comparing MDCT-derived measures of trabecular bone structure to those obtained by μ CT (Fig. 2) showed significant differences for all parameters and protocols except for Tb.N in protocol A and Tb.Sp in protocol C (Table 1). App. BV/TV was 4- to 5-fold higher and app. Tb.Th was 3-fold higher than the corresponding standard measures determined by μ CT, suggesting a significant overestimation of those structure measures when determined by MDCT. App. Tb.Sp and app. Tb.N were both slightly underestimated in the standard protocol B. For protocol A, app. Tb.Sp, and for protocol C, app. Tb. N was significantly underestimated.

The highest, yet overall moderate correlations between MDCT-derived apparent structure measures and μ CT were found for BV/TV, reaching R^2 values of 0.64 (*p* < 0.0001) for MDCT protocol B, followed by only low correlations for Tb.Th (R^2 = 0.32–0.36, *p* < 0.01; Table 2). Small correlations were found for Tb.Sp (R^2 = 0.25 and 0.19) and Tb.N (R^2 = 0.15 and 0.13) as assessed with MDCT protocols B and C.

Correlations between MDCT-derived texture measures and μ CT-derived structural parameters

Of all derived texture measures, only the highest correlations between MDCT-derived texture measures and μ CT-derived structure measures are listed in Table 3. Interestingly for vBMD and BV/TV, as well as for Tb.Sp, Tb.N, and Conn.D, the same texture measure categories were found to compute the best correlations. For vBMD and BV/TV, this texture category was the scaling index method category (SIM_{quan75.r8}), with R^2 values of up to 0.70 (*p* < 0.0001). For Tb.Sp, Tb.N, and Conn.D, measures of TOGLCM_{LNE} yielded the highest R^2 values for protocols B and C. Tb.Th correlated best with the MD measure MD_{deg45} (R^2 = 0.42, *p* < 0.01).

Correlations between MDCT- and μ CT-derived measures to biomechanical properties

Linear regression analysis: The highest but moderate correlation for a single parameter with μ FE modeling was obtained for the various measures of BMD. App. modulus reached an R^2 of 0.60 (*p* < 0.001) with QCT-derived BMD (Table 4) and stiffness reached an R^2 of 0.66 (*p* < 0.001)

TABLE 4. Coefficients of Determination (R^2) Calculated Using Linear Regression Analysis (Single)

	μ FE app. modulus							
	MDCT protocol							
	A		B		C			
	QCT	μ CT	Single	Multi	Single	Multi	Single	Multi
N = 33								
BMD	0.60*	—	—	0.75* ⁵	—	0.73* ⁴	—	0.72* ⁴
vBMD	—	0.58*	0.40*	NS	0.58*	0.67* ⁹	0.53*	0.63* ⁸
BV/TV	—	0.44*	0.46*	<BMD	0.58*	0.65* ⁹	0.56*	0.66* ⁸
Tb.Th	—	0.17 [‡]	0.41*	<BMD	0.46*	0.71* ¹¹	0.40*	<BMD
Tb.Sp	—	NS	NS	<BMD	0.36*	<BMD	0.42*	<BMD
Tb.N	—	NS	NS	<BMD	NS	<BMD	0.24 [†]	<BMD
Conn.D	—	NS	—	—	—	—	—	—
SMI	—	0.44*	—	—	—	—	—	—
MF _{area.qu25}	—	—	NS	—	0.42*	—	0.37*	—

A multivariate linear regression model was chosen to combine each bone structure parameter and vBMD with an additional texture measure (multi). Multivariate regression models with a weaker correlation (<0.60) than the linear regression for QCT-derived BMD (<BMD).

MDCT protocol A: 80 kVp, 150 mA; B: 120 kVp, 250 mA; C: 135kVp, 350 mA.

* $p < 0.001$.

† $p < 0.01$.

‡ $p < 0.05$.

Minkowski functionals (MF): ¹MF_{area.qu75}, ²MF_{euler.qu50}, ³MF_{perim.qu75}.

Minkowski dimension (MD): ⁴MD_{deg0}, ⁵MD_{aniso.std}.

Scaling index method (SIM): ⁶SIM_{quan25.r4}, ⁷SIM_{quan25.r6}, ⁸SIM_{quan75.r4}, ⁹SIM_{quan75.r6}, ¹⁰SIM_{quan90.r4}, ¹¹SIM_{quan90.r6}, ¹²SIM_{stedv.r4}, ¹²SIM_{median.r6}.
NS, nonsignificant.

with μ CT-derived vBMD (Table 5). Correlations with stiffness and μ CT-derived BV/TV and SMI were also only moderate ($R^2 = 0.58$ and 0.49 , $p < 0.001$). Altogether, Tb.Th, Tb.Sp, Tb.N, and Conn.D showed little to no correlation with stiffness and apparent modulus.

For MDCT-derived measures, vBMD and app. BV/TV showed the strongest correlations to μ FE stiffness and apparent modulus. MDCT protocol B- and C-derived app. Tb.Sp and app. Tb.N showed moderate to little correlations with the μ FE models for elastic modulus ($R^2 = 0.42$ and 0.24 , respectively) and stiffness ($R^2 = 0.49$ and 0.29 , respectively) compared with μ CT-derived Tb.Sp and Tb.N, which were both nonsignificant. Concerning app. Tb.Th and its relationship to μ FE, it is noteworthy that higher and better correlations were found compared with the μ CT-derived Tb.Th measures; this may be because of the MDCT-dependent overestimation. The MFs measure MF_{area.qu25} was found to be the strongest texture correlate against biomechanical measures; however, this only applied to protocols B and C. All other texture parameters did not show significant correlations to biomechanical properties.

Multivariate regression model: Stepwise multivariate regression analysis was used to identify two combined parameters that gave improved prediction of bone strength compared with QCT-derived BMD. Combining MDCT-derived vBMD with MDCT-derived structure measures did not yield significant correlations to μ FE app. modulus or stiffness for any of the protocols. Combining MDCT-

TABLE 5. Coefficients of Determination (R^2) Calculated Using Linear Regression Analysis (Single)

	μ FE stiffness							
	MDCT protocol							
	A		B		C			
	QCT	μ CT	Single	Multi	Single	Multi	Single	Multi
(N = 33)								
BMD	0.63*	—	—	0.76* ⁵	—	0.73* ³	—	0.73* ⁴
vBMD	—	0.66*	0.44*	NS	0.62*	NS	0.61 ^c	NS
BV/TV	—	0.58*	0.50*	NS	0.63*	0.72* ¹¹	0.63*	0.68* ¹⁰
Tb.Th	—	0.12 [‡]	0.41*	<BMD	0.48*	0.75* ¹¹	0.42*	<BMD
Tb.Sp	—	NS	0.15 ^a	<BMD	0.44*	<BMD	0.49*	<BMD
Tb.N	—	NS	NS	<BMD	0.14 [‡]	<BMD	0.29 [†]	<BMD
Conn.D	—	NS	—	—	—	—	—	—
SMI	—	0.49*	—	—	—	—	—	—
MF _{area.qu25}	—	—	NS	—	0.41*	—	0.43*	—

A multivariate linear regression model was chosen to combine each bone structure parameter and vBMD with an additional texture measure (multi). Multivariate regression models with a weaker correlation (<0.63) than the linear regression for QCT BMD (<BMD).

MDCT protocol A: 80 kVp, 150 mA; B: 120 kVp, 250 mA; C: 135kVp, 350 mA.

* $p < 0.001$.

† $p < 0.01$.

‡ $p < 0.05$.

Minkowski functionals (MF): ¹MF_{area.qu75}, ²MF_{euler.qu50}, ³MF_{perim.qu75}.

Minkowski dimension (MD): ⁴MD_{deg0}, ⁵MD_{aniso.std}.

Scaling index method (SIM): ⁶SIM_{quan25.r4}, ⁷SIM_{quan25.r6}, ⁸SIM_{quan75.r4}, ⁹SIM_{quan75.r6}, ¹⁰SIM_{quan90.r4}, ¹¹SIM_{quan90.r6}, ¹²SIM_{stedv.r4}, ¹²SIM_{median.r6}.
NS, nonsignificant.

derived vBMD with one of MDCT-derived texture measures improved the correlation with μ FE apparent modulus within protocols B and C only minimally, but yielded a lower level of significance (Table 4). Combining MDCT-derived app. Tb.Th with the SIM measure SIM_{quan90.r6} improved the correlation with apparent modulus ($R^2 = 0.71$; QCT BMD: $R^2 = 0.60$, $p < 0.001$) and stiffness ($R^2 = 0.75$; QCT BMD: $R^2 = 0.63$, $p < 0.001$) over QCT-derived BMD. Overall, the strongest correlations to biomechanical properties were found by combining QCT-derived BMD with MD_{aniso.std} (protocol A, $R^2 = 0.76$ against stiffness) and MD_{deg0} (protocol C, $R^2 = 0.72$, μ FE app. elastic modulus).

DISCUSSION

The aim of this study was to evaluate the accuracy of trabecular bone structure analysis applied to spinal MDCT images acquired in an in vivo-like setup, using μ CT as the standard of reference. Our results show that trabecular bone structure measures of the osteoporotic spine, as derived from MDCT images, show limited, yet significant correlations with trabecular bone structure measures as assessed by μ CT. Furthermore, our results suggest that texture measures in combination with BMD correlate better with μ FE biomechanical properties compared with single measures of structure alone.

For the diagnosis of osteoporosis and for therapy monitoring, it has been well accepted that BMD can only

partially explain bone strength and that the evaluation of bone microarchitecture enhances the prediction of biomechanical properties.^(8,38,39) With the introduction of HR-pQCT (82- μ m isotropic voxel size), peripheral sites such as the distal radius and the distal tibia are now accessible for trabecular bone imaging in vivo.^(13,40) Nonetheless, in vivo imaging of critical central skeletal sites such as the spine and the proximal femur remain a challenge. In the field of trabecular bone structure analysis, the presented MDCT study is the first to simulate in vivo patient examination of the spine validating derived structure measures with μ CT as the standard of reference.

Consistent with previous studies, the highest correlation between MDCT-derived apparent structure measures and μ CT-derived structure measures was found for BV/TV. Bauer et al.⁽⁴¹⁾ reported correlations up to 0.84 (Pearson) for app. BV/TV measured in a simulated soft tissue environment. Higher correlations of $R^2 = 0.84$ were found in a study on 20 vertebral bone specimens; however, imaging was performed without the surrounding soft tissue.⁽⁴²⁾ Thus, our results for in situ MDCT (MDCT versus μ CT for BV/TV, $R^2 = 0.52$ – 0.64 , $r_{\text{pearson}} = 0.72$ – 0.80) are well within the expected range. Apart from BV/TV, the only significant, yet low correlation among structure measures was found for Tb.Th ($R^2 = 0.32$ and 0.36). Correlations for Tb.Sp and Tb.N were substantially weaker and little ($R^2 = 0.13$ – 0.25). Interestingly, these results differ substantially from the study conducted by Bauer et al.,^(41,42) where the weakest correlations were found for Tb.Th, whereas Tb.N and Tb.Sp yielded r_{pearson} correlations of 0.76 and 0.79. We hypothesize that this may be caused by an overrepresentation of large but few trabeculae, because our donors were predominantly in the osteoporotic range. Therefore, imaging sparse trabecular microarchitecture using the MDCT system under clinical conditions (average in plane pixel size of 0.274 mm^2 and slice thickness of 0.500 mm) is likely limited to capturing only the thickest trabeculae within the network.

Overall, considering that (1) app. BV/TV is only a surrogate density measure and (2) Tb.Th, Tb.Sp, and Tb.N only have limited correlations with their corresponding μ CT measures, our results suggest that trabecular bone of the osteoporotic spine, as depicted by MDCT, only partially reflects the true bone structure. As expected, our results do show that the assessment of BMD within a volume of interest is quite robust (μ CT versus MDCT: $R^2 = 0.86$, $p < 0.0001$). Additionally, an increase in dosage (from 120 kVp and 250 mA [protocol B] to 135 kVp and 350 mA [protocol C]) did not lead to a substantial improvement in the accuracy of trabecular bone measures.

Several studies assessing trabecular structure in vivo have been published using clinical MDCT scanners.^(14,15,43–46) Most recently, Graeff et al.⁽¹⁵⁾ evaluated the feasibility of MDCT-based trabecular bone structure analysis to quantify longitudinal effects of teriparatide on microarchitectural changes. A cohort of 65 postmenopausal women was monitored during a 12-mo treatment period. Structural parameters such as app. BV/TV and app. Tb.N increased significantly ($30.6 \pm 4.4\%$ and $19.0 \pm 3.2\%$, respectively) and were partially independent from

changes in BMD. The authors concluded that HR-CT is a feasible in vivo method to quantify changes in trabecular microarchitecture in the human spine. However, no gold standard correlation was obtained, so it will remain unknown what amount of the true trabecular network was assessed.

In a study performed by Ito et al.⁽¹⁴⁾ on 82 postmenopausal women, it was shown that evaluation of MDCT-derived SMI and app. BV/TV in L₃ had a higher relative risk (OR, 16.0 and 13.6, respectively) for preexisting vertebral fractures than DXA-based BMD measures alone (OR, 4.8). Although in this study comparative scans between MDCT and μ CT were additionally performed on excised vertebral spine specimens, it needs to be considered that image quality would be expected to be positively biased with the exclusion of peripheral soft tissue and bone. Accordingly, the strong correlation to BV/TV ($r = 0.98$, $p < 0.005$) is not directly translatable to true in vivo conditions where significantly lower SNR and patient motion compromise image quality.

The depiction of the trabecular network using MDCT is limited by different factors. The first, and probably most important factor, is spatial resolution. The mean trabecular thickness of the vertebrae investigated in this study was 0.160 mm , whereas the nominal in-plane pixel size was $\sim 0.274 \text{ mm}$. It is obvious that trabeculae smaller than the resolution will be poorly depicted and represent a significant segmentation challenge. Even for high-resolution devices with far finer pixel size, resolution-dependent variations of trabecular parameters can be observed.⁽⁴⁷⁾ For standard clinical devices such as MDCT, resolution is constrained by radiation dose and SNR considerations.

Second, image quality of MDCT scans of the spine is clearly diminished by noise. Beam hardening characteristics and signal-to-noise ratio are strongly affected by the amount of surrounding soft tissue in the tomography plane.⁽⁴¹⁾ Thus, for central skeletal sites such as the spine and the proximal femur, constraints in contrast and image homogeneity would be expected to limit trabecular bone depiction and analysis. Bauer et al.⁽⁴¹⁾ investigated the influence of a simulated soft tissue environment on high-resolution MDCT-derived trabecular structure analysis, using μ CT as a standard of reference. Trabecular structure measures obtained from scans with a simulated soft tissue environment yielded lower correlations to μ CT compared with scans without the simulated soft tissue environment ($r = 0.84$ versus $r = 0.90$ for app. BV/TV). They concluded that, although surrounding soft tissue at central sites compromises image quality, major characteristics of the trabecular network might still be depicted and quantified. Although this study was designed close to in vivo scan conditions, an adoption of the results to actual clinical patient scans may be limited, because all scans were performed with one static soft tissue phantom implementing ideal scan parameters. In an attempt to create an experimental setup that more realistically evaluates the ability of MDCT-derived trabecular bone measures to reflect the true trabecular bone structure, our study was conducted on intact, unfixed body donors within a few days after their death.

In terms of investigating the relationship with elastic biomechanical properties, the results of our linear regression analysis found that only BV/TV and SMI were significantly correlated to apparent modulus and stiffness. This result is in full accordance to a recently published study by Arlot et al.,⁽⁴⁸⁾ in which BV/TV and SMI were both identified to be superior to Tb.Th, Tb.Sp, Tb.N, and Conn.D in predicting microdamage. They were able to show that, in human vertebral cancellous bone, microdamage is associated with low BV/TV and a rod-like trabecular architecture, showing that 35% of variance in microcrack density and 20% of the variance in diffuse damage accumulation are associated with the SMI. In a set of four femoral head specimens, Ito et al.⁽¹⁴⁾ also identified MDCT derived app. BV/TV, SMI and app. Tb.N to correlate significantly with ultimate load. Nevertheless, of all parameters, BMD measures were the single strongest predictors of biomechanical properties determined by μ FE. Multivariate regression analysis showed that the largest improvement for the correlation with stiffness was achieved by combining QCT-derived BMD with MD texture measures, followed by a combination of app. BV/TV and app. Tb.Th (MDCT protocol B) with the SIM-associated texture measures. Collectively, this suggests that, at currently achievable in vivo image quality profiles, analysis of texture measures may hold greater potential to improve BMD-based bone quality assessment compared with direct assessment of the trabecular structure. This finding is in accordance with previously published data that have shown that trabecular texture measures show significant correlations with trabecular structure measures and may be used to estimate bone strength and to differentiate patients with and without fractures.^(49–52)

In summary, we performed structure and texture analysis of the lumbar spine in intact human cadavers and compared these with corresponding μ CT and μ FE measures. The following conclusions may be drawn from our results: (1) MDCT-derived structure measures obtained in osteoporotic lumbar spines show limited, yet significant correlations with μ CT-derived trabecular bone structure, (2) MDCT-derived density measures in osteoporotic spines show highly significant correlations with trabecular BMD, (3) MDCT-derived density measures show the highest correlations with μ FE models for stiffness and app. elastic modulus, and (4) a combination with MDCT-derived texture measures improves the correlations substantially compared with single measures of trabecular bone structure.

ACKNOWLEDGMENTS

This study was funded by the Elsbeth Bonhoff grant (Charité 898 32 232).

REFERENCES

- Cummings SR 1985 Are patients with hip fractures more osteoporotic? Review of the evidence. *Am J Med* **78**:487–494.
- Ott SM 1993 When bone mass fails to predict bone failure. *Calcif Tissue Int* **53**(Suppl 1):S7–S13.
- Siris ES, Chen YT, Abbott TA, Barrett-Connor E, Miller PD, Wehren LE, Berger ML 2004 Bone mineral density thresholds for pharmacological intervention to prevent fractures. *Arch Intern Med* **164**:1108–1112.
- Cummings SR, Karpf DB, Harris F, Genant HK, Ensrud K, LaCroix AZ, Black DM 2002 Improvement in spine bone density and reduction in risk of vertebral fractures during treatment with antiresorptive drugs. *Am J Med* **112**:281–289.
- Riggs BL, Melton LJ III 2002 Bone turnover matters: The raloxifene treatment paradox of dramatic decreases in vertebral fractures without commensurate increases in bone density. *J Bone Miner Res* **17**:11–14.
- Sarkar S, Mitlak BH, Wong M, Stock JL, Black DM, Harper KD 2002 Relationships between bone mineral density and incident vertebral fracture risk with raloxifene therapy. *J Bone Miner Res* **17**:1–10.
- Bouxsein ML 2003 Bone quality: Where do we go from here? *Osteoporos Int* **14**(Suppl 5):S118–S127.
- Seeman E, Delmas PD 2006 Bone quality—the material and structural basis of bone strength and fragility. *N Engl J Med* **354**:2250–2261.
- Kleerekoper M, Villanueva AR, Stanciu J, Rao DS, Parfitt AM 1985 The role of three-dimensional trabecular microstructure in the pathogenesis of vertebral compression fractures. *Calcif Tissue Int* **37**:594–597.
- McDonnell P, McHugh PE, O'Mahoney D 2007 Vertebral osteoporosis and trabecular bone quality. *Ann Biomed Eng* **35**:170–189.
- Silva MJ 2007 Biomechanics of osteoporotic fractures. *Injury* **38**(Suppl 3):S69–S76.
- Boutroy S, Bouxsein ML, Munoz F, Delmas PD 2005 In vivo assessment of trabecular bone microarchitecture by high-resolution peripheral quantitative computed tomography. *J Clin Endocrinol Metab* **90**:6508–6515.
- Kazakia GJ, Hyun B, Burghardt AJ, Krug R, Newitt DC, de Papp AE, Link TM, Majumdar S 2008 In Vivo Determination of Bone Structure in Postmenopausal Women: A Comparison of HR-pQCT and High-Field MR Imaging. *J Bone Miner Res* **23**:463–474.
- Ito M, Ikeda K, Nishiguchi M, Shindo H, Uetani M, Hosoi T, Orimo H 2005 Multi-detector row CT imaging of vertebral microstructure for evaluation of fracture risk. *J Bone Miner Res* **20**:1828–1836.
- Graeff C, Timm W, Nickelsen TN, Farrerons J, Marin F, Barker C, Gluer CC 2007 Monitoring teriparatide-associated changes in vertebral microstructure by high-resolution CT in vivo: Results from the EUROFORs study. *J Bone Miner Res* **22**:1426–1433.
- Thomsen JS, Laib A, Koller B, Prohaska S, Mosekilde L, Gowin W 2005 Stereological measures of trabecular bone structure: Comparison of 3D micro computed tomography with 2D histological sections in human proximal tibial bone biopsies. *J Microsc* **218**:171–179.
- Muller R, Van Campenhout H, Van Damme B, Van Der Perre G, Dequeker J, Hildebrand T, Rueggsegger P 1998 Morphometric analysis of human bone biopsies: A quantitative structural comparison of histological sections and micro-computed tomography. *Bone* **23**:59–66.
- Rueggsegger P, Koller B, Muller R 1996 A microtomographic system for the nondestructive evaluation of bone architecture. *Calcif Tissue Int* **58**:24–29.
- Genant HK, Wu CY, van Kuijk C, Nevitt MC 1993 Vertebral fracture assessment using a semiquantitative technique. *J Bone Miner Res* **8**:1137–1148.
- Majumdar S, Genant HK 1997 Assessment of trabecular structure using high resolution magnetic resonance imaging. *Stud Health Technol Inform* **40**:81–96.
- Ridler TW 1978 Picture Thresholding Using an Iterative Selection Method. *IEEE Trans Syst Man Cybern* **8**:630–632.
- Odgaard A 1997 Three-dimensional methods for quantification of cancellous bone architecture. *Bone* **20**:315–328.

23. Hildebrand T, Ruegsegger P 1997 Quantification of bone microarchitecture with the structure model index. *Comput Methods Biomech Biomed Engin* **1**:15–23.
24. Hildebrand T, Laib A, Muller R, Dequeker J, Ruegsegger P 1999 Direct three-dimensional morphometric analysis of human cancellous bone: Microstructural data from spine, femur, iliac crest, and calcaneus. *J Bone Miner Res* **14**:1167–1174.
25. Jiang C, Giger ML, Chinander MR, Martell JM, Kwak S, Favus MJ 1999 Characterization of bone quality using computer-extracted radiographic features. *Med Phys* **26**:872–879.
26. Maragos P 1994 Fractal signal analysis using mathematical morphology. *Adv Electron Electron Phys* **88**:199–246.
27. Boehm HF, Link TM, Monetti RA, Kuhn V, Eckstein F, Raeth CW, Reiser M 2006 Analysis of the topological properties of the proximal femur on a regional scale: Evaluation of multi-detector CT-scans for the assessment of biomechanical strength using Local minkowski functionals in 3D. *Proc SPIE* **6144**:61446x7–61446x8.
28. Boehm HF, Vogel T, Panteleon A, Burklein D, Bitterling H, Reiser M 2007 Differentiation between post-menopausal women with and without hip fractures: Enhanced evaluation of clinical DXA by topological analysis of the mineral distribution in the scan images. *Osteoporos Int* **18**:779–787.
29. Haralick RM, Shanmugam K, Dinstein I 1973 Textural features for image classification. *IEEE Trans Syst Man Cybern* **3**:610–621.
30. Anys H, He DC 1995 Evaluation of textural and multi-polarization radar features for crop classification. *IEEE Trans Geosci Rem Sens* **33**:1170–1181.
31. Boehm HF, Raeth C, Monetti RA, Mueller D, Newitt D, Majumdar S, Rummeny E, Morfill G, Link TM 2003 Local 3D scaling properties for the analysis of trabecular bone extracted from high-resolution magnetic resonance imaging of human trabecular bone: Comparison with bone mineral density in the prediction of biomechanical strength in vitro. *Invest Radiol* **38**:269–280.
32. Jamitzky F, Stark RW, Bunk W, Thalhammer S, Rath C, Aschenbrenner T, Morfill GE, Heckl WM 2001 Scaling-index method as an image processing tool in scanning-probe microscopy. *Ultramicroscopy* **86**:241–246.
33. Pompl R, Bunk W, Horst A, Stolz W, Abmayr W, Brauner W, Glaessl A, Morfill G 2000 MELDOQ: Ein System zur Unterstützung der Früherkennung des malignen Melanoms durch digitale Bildverarbeitung. *Bildverarbeitung für die Medizin*. Springer, Berlin, Germany.
34. Muller R, Ruegsegger P 1995 Three-dimensional finite element modelling of non-invasively assessed trabecular bone structures. *Med Eng Phys* **17**:126–133.
35. Van Rietbergen B, Weinans H, Huiskes R, Odgaard A 1995 A new method to determine trabecular bone elastic properties and loading using micromechanical finite-element models. *J Biomech* **28**:69–81.
36. Van Rietbergen B, Odgaard A, Kabel J, Huiskes R 1996 Direct mechanics assessment of elastic symmetries and properties of trabecular bone architecture. *J Biomech* **29**:1653–1657.
37. Felsenberg D, Gowin W 1999 [Bone densitometry by dual energy methods]. *Radiologe* **39**:186–193.
38. Ammann P, Rizzoli R 2003 Bone strength and its determinants. *Osteoporos Int* **14**(Suppl 3):S13–S18.
39. Yeni YN, Brown CU, Wang Z, Norman TL 1997 The influence of bone morphology on fracture toughness of the human femur and tibia. *Bone* **21**:453–459.
40. MacNeil JA, Boyd SK 2007 Accuracy of high-resolution peripheral quantitative computed tomography for measurement of bone quality. *Med Eng Phys* **29**:1096–1105.
41. Bauer JS, Link TM, Burghardt A, Henning TD, Mueller D, Majumdar S, Prevrhal S 2007 Analysis of trabecular bone structure with multidetector spiral computed tomography in a simulated soft-tissue environment. *Calcif Tissue Int* **80**:366–373.
42. Bauer JS, Issever AS, Fischbeck M, Burghardt A, Eckstein F, Rummeny EJ, Majumdar S, Link TM 2004 [Multislice-CT for structure analysis of trabecular bone: A comparison with micro-CT and biomechanical strength]. *Rofo* **176**:709–718.
43. Chevalier F, Laval-Jeantet AM, Laval-Jeantet M, Bergot C 1992 CT image analysis of the vertebral trabecular network in vivo. *Calcif Tissue Int* **51**:8–13.
44. Gordon CL, Lang TF, Augat P, Genant HK 1998 Image-based assessment of spinal trabecular bone structure from high-resolution CT images. *Osteoporos Int* **8**:317–325.
45. Ito M, Ohki M, Hayashi K, Yamada M, Uetani M, Nakamura T 1995 Trabecular texture analysis of CT images in the relationship with spinal fracture. *Radiology* **194**:55–59.
46. Munding A, Wiesmeier B, Dinkel E, Helwig A, Beck A, Schulte Moenting J 1993 Quantitative image analysis of vertebral body architecture—improved diagnosis in osteoporosis based on high-resolution computed tomography. *Br J Radiol* **66**:209–213.
47. Muller R, Koller B, Hildebrand T, Laib A, Gianolini S, Ruegsegger P 1996 Resolution dependency of microstructural properties of cancellous bone based on three-dimensional mu-tomography. *Technol Health Care* **4**:113–119.
48. Arlot ME, Burt-Pichat B, Roux JE, Vashishth D, Bouxsein ML, Delmas PD 2008 Microarchitecture influences micro-damage accumulation in human vertebral trabecular bone. *J Bone Miner Res* **23**:1613–1618.
49. Apostol L, Boudousq V, Basset O, Odet C, Yot S, Tabary J, Dinten JM, Boiler E, Kotzki PO, Peyrin F 2006 Relevance of 2D radiographic texture analysis for the assessment of 3D bone micro-architecture. *Med Phys* **33**:3546–3556.
50. Lin JC, Grampp S, Link T, Kothari M, Newitt DC, Felsenberg D, Majumdar S 1999 Fractal analysis of proximal femur radiographs: Correlation with biomechanical properties and bone mineral density. *Osteoporos Int* **9**:516–524.
51. Pothuaud L, Carceller P, Hans D 2008 Correlations between grey-level variations in 2D projection images (TBS) and 3D microarchitecture: Applications in the study of human trabecular bone microarchitecture. *Bone* **42**:775–787.
52. Vokes TJ, Giger ML, Chinander MR, Karrison TG, Favus MJ, Dixon LB 2006 Radiographic texture analysis of densitometer-generated calcaneus images differentiates postmenopausal women with and without fractures. *Osteoporos Int* **17**:1472–1482.

Received in original form November 13, 2008; revised form January 23, 2009; accepted March 25, 2009.